Journal of Fluids and Structures (1997) **11,** 89–109

NONLINEAR BEHAVIOR OF A TYPICAL AIRFOIL SECTION WITH CONTROL SURFACE FREEPLAY: A NUMERICAL AND EXPERIMENTAL STUDY

M. D. Conner, D. M. Tang, E. H. Dowell, and L. N. Virgin
Department of Mechanical Engineering and Materials Science, Duke University Durham, NC 27708-0300, U.S.A.

(Received 8 March 1996 and in revised form 25 July 1996)

A three degree-of-freedom aeroelastic typical section with control surface freeplay is modeled theoretically as a system of piecewise linear state-space models. The system response is determined by time marching of the governing equations using a standard Runge–Kutta algorithm in conjunction with Hénon's method for integrating a system of equations to a prescribed surface of phase space section. Hénon's method is used to locate the "switching points" accurately and efficiently as the system moves from one linear region into another. An experimental model which closely approximates the three degree-of-freedom typical section in two-dimensional, incompressible flow has been created to validate the theoretical model. Consideration is given to modeling realistically the structural damping present in the experimental system. The effect of the freeplay on the system response is examined numerically and experimentally. The development of the state–space model offers a low-order, computationally efficient means of modeling fully the freeplay nonlinearity and may offer advantages in future research which will investigate the effects of freeplay on the control of flutter in the typical section.

1. INTRODUCTION

Early theoretical studies of aeroelastic systems with structural freeplay were carried out on analog computers (Woolston *et al.* 1955, 1957; McIntosh *et al.* 1981), by linearizing the system about the nonlinearity via describing functions or harmonic balance (Shen 1959; Breitbach 1977; Laurenson & Trn 1980; Yang & Zhao 1988; Hauenstein *et al.* 1992, Tang & Dowell 1992, Price *et al.* 1995), or by time marching integration (Lee & LeBlanc 1986; Lee & Desrochers 1987; Yang & Zhao 1988; Kousen & Bendiksen 1994; Price *et al.* 1994, 1995). One of the compelling advantages of using harmonic balance or describing functions for aeroelastic systems is that traditional linear analytical tools, such as eigenanalysis, can be used for the determination of system stability while still allowing for the prediction of some nonlinear behavior. However, the response of a true nonlinear system may be dependent on the initial conditions, and the describing function approach does not permit a full exploration of this effect. The dependence on initial conditions and the wide variety of nonlinear behavior exhibited by systems with freeplay show the importance of incorporating this common physical nonlinearity into the theoretical model. In addition, the freeplay nonlinearity will likely have a significant effect on the response of the system to a control law designed for the nominal linear system.

A theoretical model capable of incorporating the full effects of the structural nonlinearity without sacrificing computational ease and efficiency is desirable. The

0889–9746/97/010089 + 21 $25.00/fl960068

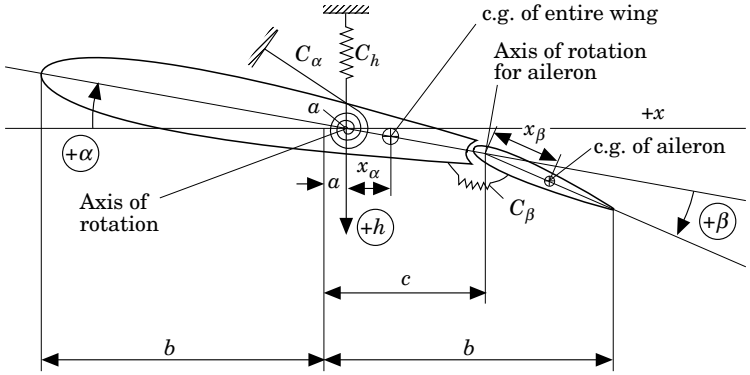

Figure 1. Schematic of the aeroelastic typical section with control surface.

describing function approach falls short of this goal for two primary reasons: (i) depending on the type of nonlinearity being considered, a significant amount of analytical work may be required to develop the form of the describing function prior to actually building the numerical model; and (ii) this technique requires the assumption that system motion will be harmonic, thus disallowing any non-periodic and transient solutions. As a result of the harmonic assumption, periodic limit cycle behavior is the only type of nonlinear solution that can be predicted. It should be noted that higher-order harmonic terms can be retained in the harmonic balance model, allowing for periodic responses other than simple harmonic motion.

The theoretical model which has been developed here is based on the state-space model proposed by Edwards *et al.* (1979) for the three degree-of-freedom aeroelastic typical section shown in Figure 1. Since the freeplay nonlinearity produces a piecewise linear change in the structural stiffness of the control surface, as shown in Figure 2, the overall system can be represented as a nonlinear combination of three linear systems. The response can be determined via numerical integration, updating the equations of

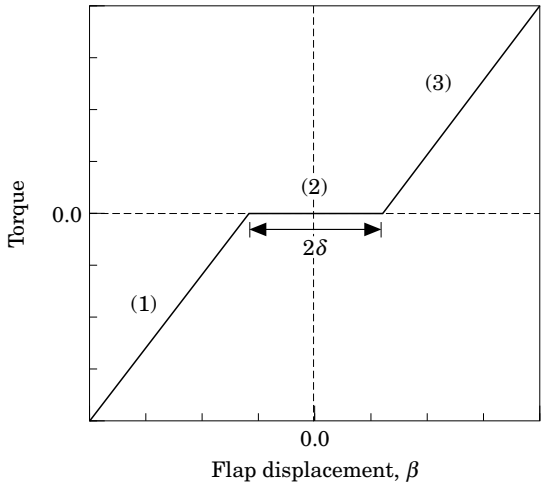

Figure 2. Restoring moment due to K_β with a symmetric freeplay region about $\beta = 0$. δ is defined as the size of the freeplay region.

motion as the system moves from one linear region into the next. It is crucial that the system be integrated to the exact point where the change in stiffness occurs. The importance of locating this ''switching point'' was addressed by Lin & Cheng (1993a, b). In those references, a similar state–space model was developed using an alternative integration scheme. Comparisons were made with the results of a describing function approach, but no experimental verification was given.

An experimental model designed to simulate the three degree-of-freedom aeroelastic typical section in two-dimensional, incompressible flow has also been developed. Nonlinear flutter phenomena including limit-cycle oscillations and chaotic motion in a typical two or three degree-of-freedom airfoil with a freeplay structural nonlinearity in wing torsion or control surface rotation have been studied theoretically by several authors. Wind tunnel flutter model tests to validate nonlinear aeroelastic theory and establish nonlinear flutter trends have also been conducted. The results from these theoretical and experimental investigations are given in Woolston *et al.* (1957), Breitbach (1977), McIntosh *et al.* (1981), Turner (1982), Yang & Zhao (1988), Lee & Tron (1989), Tang & Dowell (1992), Kousen & Bendiksen (1994) and Price *et al.* (1994).

In incompressible two-dimensional flow, limit-cycle oscillations and chaotic motion were obtained for airspeeds well below the linear flutter boundary for a two-dimensional airfoil with a freeplay nonlinearity in torsion. The limited amplitude flutter was strongly dependent on the initial conditions of the airfoil (McIntosh *et al.* 1981; Yang & Zhao 1988; Lee & Tron 1989; Tang & Dowell 1992; Price *et al.* 1994).

The goals of the present experimental work are to:

(a) experimentally study limited amplitude flutter behavior for a three degree-of-freedom airfoil subject to two-dimensional incompressible flow with a structural freeplay nonlinearity in the control surface;
(b) develop an experimental model that is capable of producing high-quality measurement data;
(c) examine theoretical/experimental correlation for evaluating a new prediction method;
(d) provide a foundation for experimental studies into the control of systems with freeplay nonlinearities.

2. STATE-SPACE MODEL

The equations of motion for the three degree-of-freedom typical section are cast in the state–space form proposed by Edwards *et al.* (1979). This format, shown in equation (1), includes two ''augmented'' states required for Jones' approximation of Wagner's indicial loading function which yields an approximation to the generalized Theodorsen function. Since the aeroelastic typical section has three degrees of freedom, there are six structural states in addition to the two augmented aerodynamic states. Therefore, $\mathbf{A}$ is an 8×8 matrix, which can be handled easily numerically. The quantity $\mathbf{a}$ represents a constant offset vector which is used in the freeplay model. The offset is required due to the fact that the curves for the restoring moment in the stiffer regions [regions (1) and (3) in Figure 2] do not pass through the origin. The state–space model is

$$\dot{\mathbf{x}} = \mathbf{A}\mathbf{x} + \mathbf{B}u + \mathbf{a}, \tag{1}$$

where $\mathbf{B}$ is the control coefficient matrix and u is the scalar command input.

The general form of the **A** matrix is given below, with the specific form of the submatrices given in Edwards *et al.* (1979):

$$\mathbf{A} = \begin{bmatrix} \mathbf{0} & \mathbf{I} & \mathbf{0} \\ -\mathbf{M}_{\text{tot}}^{-1}\mathbf{K}_{\text{tot}} & -\mathbf{M}_{\text{tot}}^{-1}\mathfrak{B}_{\text{tot}} & \mathbf{M}_{\text{tot}}^{-1}\mathbf{D} \\ \mathbf{E}_1 & \mathbf{E}_2 & \mathbf{F}_{\text{a}} \end{bmatrix}_{8\times 8}. \tag{2}$$

The "tot" subscript represents the total values of mass, damping and stiffness, comprised of structural and aerodynamic components. For the system with freeplay, all of the components of the **A** matrix are the same in the stiff and freeplay regions except for the $\mathbf{K}_{\text{tot}}$ submatrix. In the freeplay region, the control surface provides no structural contribution to the system stiffness.

The coefficient matrix **A**, for regions (1) and (3) in Figure 2 is the same; however, the value of the offset vector, **a**, differs. Region (2) has a different coefficient matrix and offset vector. Note that preload can be incorporated through the offset vectors.

The **B** matrix is given by

$$\mathbf{B} = \begin{bmatrix} \mathbf{0} \\ \mathbf{M}_{\text{tot}}^{-1}\mathbf{G} \\ \mathbf{0} \end{bmatrix}_{8\times 1}, \tag{3}$$

where

$$\mathbf{G} = \begin{bmatrix} 0 \\ K_\beta \\ 0 \end{bmatrix}_{3\times 1}. \tag{4}$$

The input, u, is a scalar command input to the flap specifying position. The full state vector, $\hat{\mathbf{x}}$, is given by

$$\hat{\mathbf{x}} = \begin{bmatrix} \mathbf{x} \\ \dot{\mathbf{x}} \\ \mathbf{x}_{\text{a}} \end{bmatrix}_{8\times 1}, \tag{5}$$

where $\mathbf{x} = [\alpha, \beta, h]^{\text{T}}$ and $\mathbf{x}_{\text{a}}$ represents the two augmented states required for the aerodynamics.

3. STRUCTURAL DAMPING MODEL

Theodorsen & Garrick (1941) examined the necessity of including at least a minimal amount of structural damping in flutter calculations. An attempt has been made here to include structural damping in the numerical model in a logical and physically meaningful way. Measurements of the structural damping present in the experimental system were made by isolating each degree of freedom, perturbing the model and recording the motion as the model returned to equilibrium in the absence of a freestream. The recorded time histories for each degree of freedom were then used to determine the corresponding damping ratio, based on logarithmic decrement calculations (Thomson 1988).

A one-term viscous damping model is used to characterize the structural damping present in the system. The dry friction in the system is assumed to be negligible. The

measured damping ratios are treated as modal damping ratios in the numerical model, which leads to the following modal damping matrix:

$$\mathfrak{B}_{\text{mod}} = \begin{bmatrix} 2m_\alpha\omega_\alpha\zeta_\alpha & 0 & 0 \\ 0 & 2m_\beta\omega_\beta\zeta_\beta & 0 \\ 0 & 0 & 2m_h\omega_h\zeta_h \end{bmatrix}_{3\times 3}, \tag{6}$$

where m represents the modal mass for each degree of freedom (per unit span), ω represents the coupled natural frequency and ζ is the measured damping ratio. The modal mass, modal stiffness and coupled natural frequencies can be calculated based on the measured mass and stiffness parameters. The modal damping matrix, $\mathfrak{B}_{\text{mod}}$, is then transformed back to the $[\alpha, \beta, h]$ coordinate system, yielding the structural portion of the total damping submatrix ($\mathfrak{B}_{\text{tot}}$). This structural damping matrix, $\mathfrak{B}_{\text{s}}$, is fully populated in general, providing coupling in the structural damping, as well as in the structural mass. The design of the experimental system is such that the coupling of the structural stiffness may be considered to be negligible.

4. NUMERICAL INTEGRATION

A key issue in the numerical integration of a piecewise linear system is accurately integrating to the "switching points" where the change in linear subdomains occurs. Hénon's method (Hénon 1982) for integrating state-space equations onto a specified surface of section has been adapted for the location of the switching points in the freeplay model. The method involves integrating the system until a change in linear subdomains is detected. At that time, the distance the system has traveled into the new subdomain is known. By exchanging the dependent variable of interest (control surface location, in this case) and independent variable, the system of equations can be integrated "in space" from its current location back to the exact point of discontinuity. This integration step yields the remaining states of the system as well as the time at which the change in subdomains occurs. At this point, time can again be made the independent variable and these values can be used along with the state–space equations for the new subdomain to integrate the system, until another discontinuity is encountered.

The details of this procedure to account for the abrupt stiffness change are given in Connor *et al.* (1996a). Hénon's method allows for the accurate location of the switching point between the linear subdomains in one integration step, as opposed to using adaptive time steps and linear interpolation or bisection (Bayly & Virgin 1991; Lin & Cheng 1993a, b).

5. STABILITY ANALYSIS

For a linear system in the form given by equation (1), the eigenvalues of the **A** matrix determine the stability of the system. As long as the real part of each eigenvalue is negative, the system is stable. When the real part of any one eigenvalue (or complex pair) becomes positive, the entire system becomes unstable. Figure 3 shows the graphical representation of the eigenanalysis in the form of a root-locus plot for the nominal linear system (without freeplay) examined in this study as the freestream velocity increases from 0 to 25 m/s, with flutter occurring at a speed of 23·9 m/s.

In contrast to the nominal linear system, there is no simple way to determine quantitatively the stability of the piecewise linear system by analysing the system

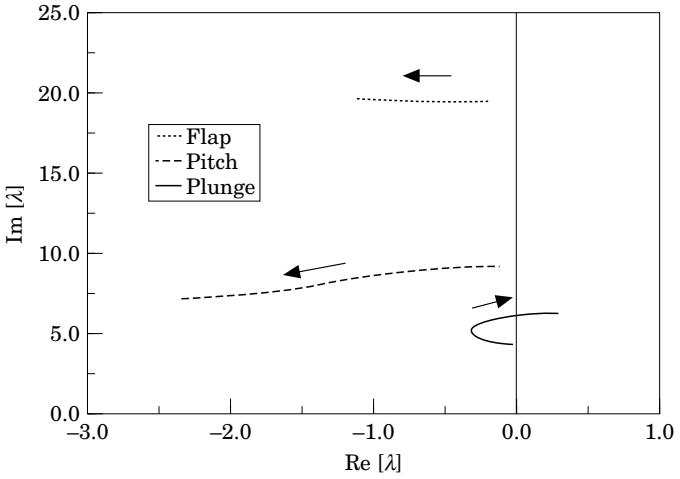

Figure 3. Root-locus plot of for the nominal linear system as the freestream velocity increases from 0 to 25 m/s. The numerical flutter velocity is 23·9 m/s and flutter frequency is 6·1 Hz.

matrices. Time-series information based on numerical integration is often used to determine the relative stability of the motion for nonlinear systems. A Poincaré map can be used to quantify the stability of limit-cycle oscillations. Once the system has reached the steady-state limit cycle, it can be perturbed, and an estimate of the Jacobian matrix based on the Poincaré section can be calculated (Dennis & Schnabel 1983; Murphy *et al.* 1994; Conner *et al.* 1996b). Linear eigenanalysis of the Jacobian matrix can then be performed to determine the relative stability of the system. This technique works very well for quantifying periodic limit cycle behavior; however, it is inappropriate for non-periodic steady-state motion.

6. DESCRIPTION OF EXPERIMENT

All flutter tests of the two-dimensional wing model with control surface freeplay were performed in the Duke University low speed wind tunnel. The wind tunnel is a closed circuit tunnel with a test-section of $0{\cdot}701\,\text{m} \times 0{\cdot}506\,\text{m}$ and a length of $1{\cdot}219\,\text{m}$. The maximum attainable air speed is 89 m/s. The stagnation temperature of the airstream is held constant over the range 15 to 38°C by means of an external air-exchange system, and tunnel stagnation pressure equals the atmospheric pressure at the low Reynolds number operating conditions. For the present test, the Reynolds number based upon model chord was $0{\cdot}52 \times 10^6$.

The flutter model is mounted in a vertical position in the center of the test-section. The clearance between the tips of the wing and the floor and ceiling of the tunnel is less than 0·32 cm. As a result, any vortical flow effects are assumed to be negligible. The vertical positioning of the model eliminates gravitational preload in the nonlinear system. A photograph of the wind tunnel model is shown in Figure 4(a).

7. FLUTTER MODEL

The two-dimensional NACA 0012 rectangular wing model includes two parts: a main wing with a 19 cm chord and 52 cm span; and a flap with a 6·35 cm chord and 52 cm span, which is mounted at the trailing edge of the main wing using two pairs of micro-bearings with a pin. The main wing is constructed from an aluminum alloy

(a)

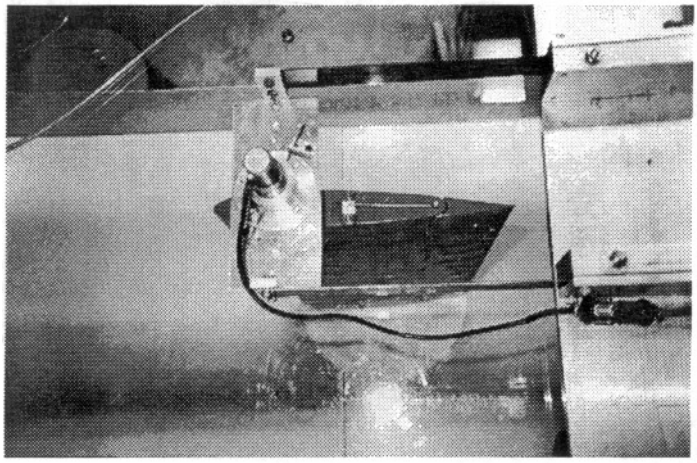

(b)

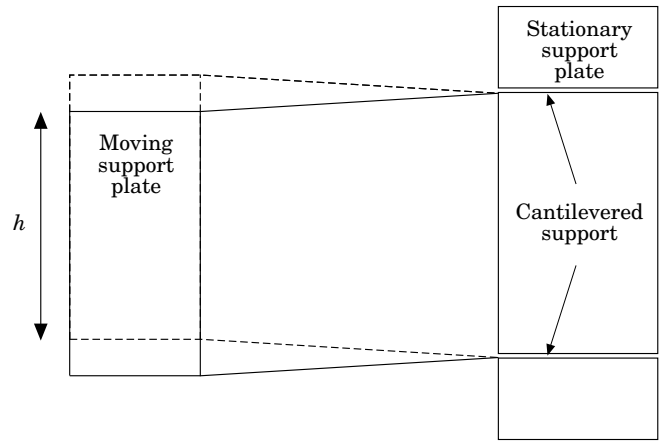

Figure 4. (a) Photograph and (b) schematic, showing top views of the experimental model and the support structure, as mounted in the Duke University low-speed wind tunnel.

circular spar beam with a diameter of 2·54 cm and a wall thickness of 0·32 cm. The beam runs through 14 pieces of NACA 0012 aluminum airfoil plate and serves as the pitch axis, located at the quarter-chord location from the leading edge. A 0·254 mm thick aluminum sheet covers the entire chord and span, providing the aerodynamic contour of the wing. In addition, an aluminum tube with 1·27 cm diameter is mounted from wing tip to wing tip at a location of 3·175 cm from the leading edge. The chordwise center of gravity can be adjusted by adding or subtracting a balance weight from this tube.

The flap is constructed in a similar manner with an aluminum alloy tube spar beam (1·27 cm diameter and 0·158 cm wall-thickness) passed through the leading edge of 14 pieces of NACA 0012 wood airfoil plate. The flap is also covered with the same type of aluminum sheet.

A rotational axis comprised of the micro-bearings and pin allows the flap to have a rotational degree of freedom relative to the main wing. A steel leaf-spring is inserted

tightly into a slot of the tube spar beam at one end of the flap. The free end of the leaf spring is inserted into a support block mounted on the main wing. The amount of structural stiffness that the leaf-spring provides can be adjusted by moving the support block toward or away from the rotational axis of the flap or by changing the diameter of the leaf-spring. Freeplay is incorporated by using a support block that allows the free end of the leaf-spring to move through a given range of motion before encountering resistance. A schematic of the leaf spring assembly for the control surface (with freeplay) is shown in Figure 5.

The support mechanisms for the entire model are mounted outside of the wind tunnel, at the top and bottom. The support mechanism at each end is a bi-cantilever beam made of two steel leaf-springs which are 20·32 cm long, 2·86 cm wide, and 0·102 cm thick. The distance between the two cantilever beams is 15·24 cm. A support block joins the free ends of the bi-cantilevered beams on both the top and the bottom and is free to move in the plunge direction. Figure 4 shows a photograph of the upper support mechanism and a schematic showing the plunging motion of the support structure. An identical structure is located on the bottom side of the wind tunnel. The two support blocks are the only parts of the support mechanism that move with the model, and this motion is restricted to the plunge degree of freedom. The pitch axis of the main wing is mounted to the upper and lower support blocks through a pair of precision bearings which have a small amount of dry friction in the ball. This design allows the model to have a plunge motion that is independent of the pitch degree of freedom. At the upper bracket, there is a spring wire inserted tightly into the pitch axis of the wing. The ends of the spring wire are simply supported on the bracket, which provides an adjustable pitch stiffness.

8. MEASUREMENT AND DATA ACQUISITION

The pitch angle of the main wing is measured by a rotational velocity displacement transducer, RVDT, which is fixed at the upper end of the pitch axis. The angular displacement transducer was calibrated and showed excellent linear response characteristics (0·26%) and high sensitivity (12% volt). The plunge displacement is measured using another RVDT which measures the motion of the upper support block. The flap rotational motion relative to the main wing is measured by a micro-RVDT which is mounted on the flap axis inside of the main wing. These three measurement signals are independent of one another.

The output from these transducers is amplified and sent to an SD 380 signal analyser and directly recorded on a MacIntosh IIci computer. The data acquisition system includes an NB-MIO-16, which consists of a 16-channel analog to digital (A/D) plug-in interface board, a BNC termination box, and LabVIEW data acquisition and analysis software. The digitized response data can be graphically displayed either on-line or off-line as a time history, phase plane plot, FFT, PSD, or Poincaré map. In order to make a comparison of the theoretical and experimental data, a measurement system calibration was completed before the wind tunnel test. The dynamic calibration coefficients were determined by a ground vibration test.

9. PRELIMINARY TEST

A preliminary test of the flutter model was used to determine the natural frequencies and the modal damping of the structure. There are four major components of the vibration test: excitation, measurement, recording and analysis. An auto-sweeping sinusoidal signal is provided by an SD 380 signal analyser. A Brüel and Kjaer (B&K)

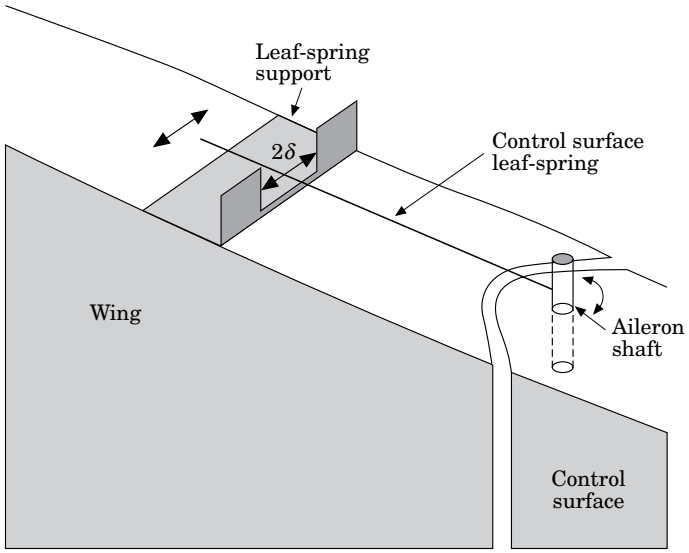

Figure 5. Schematic of a portion of the wing-aileron assembly showing the leaf spring-freeplay configuration used in the experimental model.

4810 mini-shaker and a B&K 2706 power amplifier are used to excite the model. The drive point is placed at the mid-span and the quarter-chord of the main wing section. A B&K 8200 force transducer is used to measure the force at the joint between the mini-shaker and the model. A B&K 2635 charge amplifier is used to provide signal conditioning and amplification of the force signal.

The output response signals include the plunge displacement, pitch angle of the main wing and the flap rotational motion from the three transducers. They are connected to the SD 380 input channels. A transfer-function analysis between the input force and output responses is completed by the SD 380 for the 0–50 Hz frequency range, averaging over 10 cycles and using a Hanning window. From the transfer function, the coupled natural frequencies for the pitch, plunge, and control surface motion were determined. In addition to the three primary degrees of freedom, the experimental model has the potential to exhibit a fourth degree of freedom (roll) due to out-of-phase plunging motion between the upper and lower supports. However, the results show that this motion is negligible. A complete listing of the system parameters for the experimental model is given in Table A.1 (in Appendix A).

The structural damping for the system was determined by isolating each of the three degrees of freedom and providing an initial disturbance in the absence of a freestream. The time histories of the decaying oscillations was recorded, from which standard logarithmic-decrement calculations were made (Thomson 1988). The calculated damping ratios were treated as uncoupled modal values in the numerical model, as discussed in Section 3.

10. EXPERIMENTAL FLUTTER

Prior to obtaining the results to be presented shortly, the structural inertia, stiffness, damping and frequency data for the experimental model were measured. The structural stiffnesses in the pitch and flap degrees of freedom are provided by single, small-diameter leaf-springs. The structural stiffness for the plunging motion is provided by

TABLE 1

Natural frequencies, flutter speeds and frequencies. The percentage difference is calculated relative to the experimental values

	Numerical	Experimental	% Difference
ω_α (coupled)	9·218 Hz	9·125 Hz	1·02%
ω_β (coupled)	19·442 Hz	18·625 Hz	4·39%
ω_h (coupled)	4·455 Hz	4·375 Hz	1·82%
Flutter speed	23·9 m/s	20·6 m/s	15·0%
Reduced velocity	3·249	2·825	15·0%
Flutter frequency	6·112 Hz	5·47 Hz	11·74%

two bi-cantilevered leaf springs which support the model on either end. During linear modal flutter testing, great caution must be exerted to avoid damaging the model. While uncontrolled growth in the response amplitude at or near the flutter speed is obviously undesirable, the use of physical ''stops'' to limit the range of motion can also lead to problems. The forces encountered in divergent flutter can reach very high levels, which means that the force imposed on the model by physical stops can also be quite high. The specific vulnerability in this particular experimental model is the relatively small diameter, steel-wire leaf-spring which provides torsional stiffness for the pitching motion. The forces encountered near flutter, or the forces imposed by flutter stops, may cause plastic deformation or even microscopic cracking which can change the spring stiffness characteristics.

Similar problems are also encountered during the nonlinear testing. The amplitude response curves are obtained by the path-following techniques described in Section 11.2. A complete sweep, in one direction, through the chosen range of freestream conditions typically requires a minimum of 30–45 min, during which time the model is undergoing limit-cycle oscillations. While the amplitude of the motion may be relatively small, degradations in the stiffness characteristics of the pitch-spring could also result from fatigue, as well as temperature effects. The coupled natural frequencies given in Table 1 (see Section 11) represent the values obtained prior to the nonlinear testing. These values were measured again upon completion of the linear tests and were found to be: $\omega_\alpha = 8{\cdot}125$ Hz, $\omega_\beta = 18{\cdot}25$ Hz, and $\omega_h = 4{\cdot}25$ Hz. The coupled natural frequencies have decreased by 12·3, 2·05, and 2·94%, respectively most likely due to changes in the torsional stiffness for the pitch degree of freedom, which could explain some of the discrepancy between the numerical and experimental flutter boundaries.

11. RESULTS

11.1. FLUTTER TEST OF THE LINEAR SYSTEM

The nominal values for the inertial, stiffness and damping parameters of the experimental system were measured and used as input to the numerical model. A summary of the system parameters is given in the Appendix A. A comparison of the key dynamical characteristics for the numerical and experimental systems is given in Table 1. The nonlinear results given in the following section were actually completed prior to the linear flutter tests in an attempt to prevent significant changes in the system parameters or even potential failure, should divergent flutter be encountered during the linear experimental model testing.

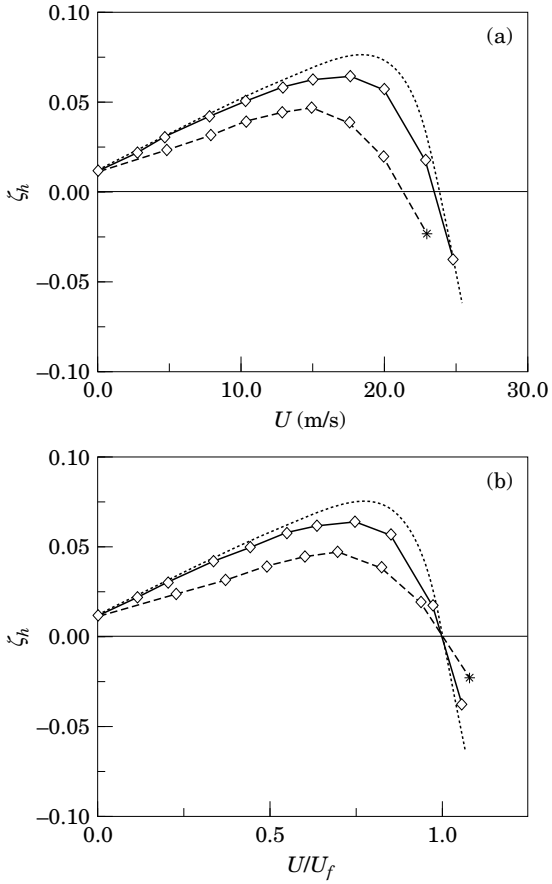

Figure 6. Average damping in the plunge mode versus (a) absolute freestream velocity and (b) fraction of respective flutter speed for the experimental system and the numerical model (based on logarithmic decrement, $\zeta \approx [\log (h_1/h_2)]/(2\pi)$), and damping based on the real part of numerical eigenvalues (normalized by the numerical in-vacuo coupled natural frequency in plunge) for the nominal linear system. · · · ·, $-\text{Re}(\lambda)/\omega_h$; —◇—, numerical log decrement; - - ◇ - -, experimental log decrement; — – —∗, extrapolated.

The measured time history data of the flutter model under an initial disturbance are recorded. For each channel, 4000 sample points of the time data are acquired. The sample rate is 800 points/s. The average damping ratio based on logarithmic decrement calculations for the plunge degree of freedom is plotted as a function of freestream velocity in Figure 6. The motion recorded in the plunge time history is not independent of the pitch and flap motion, which means that the calculated damping is a coupled value. Time history data are recorded for speeds below the predicted flutter speed.

The average modal damping values obtained for the experimental system correspond to the real part of the linear **A** matrix eigenvalues in the numerical model, though the magnitude may differ from the value determined for the experimental value of modal damping. The trends displayed by the real part of the eigenvalues and the measured damping values should be similar. Linear flutter occurs when the overall system damping becomes negative, i.e., the freestream adds energy to the system rather than dissipating energy. Figure 6(a) shows that there is approximately a 15% difference in the predicted flutter speed based on numerical eigenanalysis and the results of the experimental flutter tests. While there is some margin for error in the measurement of the experimental parameters used as input to the numerical model, the most likely

source of this error is in aerodynamic effects that are not modeled by the Theodorsen model and by three-dimensional aerodynamic effects that may be present in the wind tunnel.

Aerodynamic corrections and more complicated aerodynamic models can be incorporated into the theoretical development. One of the goals in the development of this numerical model, though, is to see how well the basic model predicts the system behavior, without corrections that are specific to the particular wing section and wind tunnel or the use of additional aerodynamic states. In order to compare the numerical and experimental results on an equivalent basis, a normalization based on the linear flutter speed has been carried out. Because nonlinearities such as freeplay are often linearized or simply ignored in theoretical models, the primary reason for the inclusion of freeplay in this numerical model is to compare the response of the system with freeplay to the ''same'' system without freeplay. Therefore, the freestream velocities have been normalized by the respective linear flutter speed for each model. Figure 6(a) shows the damping in the plunge mode of the linear system as a function of absolute freestream velocity. Figure 6(b) shows the same information after normalizing the velocity scale for each curve by its respective measured linear flutter speed (or predicted flutter speed).

Figure 6 shows three curves representing the log decrement calculations based on the plunge mode for the experimental and numerical models, as well as the real portion of the numerical eigenvalue for the plunge mode, normalized with respect to the *in vacuo* coupled natural frequency for plunge. The plunge modal damping increases and then decreases as the velocity increases. There is a damping maximum in all three curves around 70–80% of their respective linear flutter speed, as shown in Figure 6(b). The structural portion of the damping is of the order of 1% (of critical) throughout the range of freestream conditions. The maximum experimental damping value is about 4%, which is dominated by the aerodynamic damping. The damping change near the divergent flutter velocity is abrupt, and the final point on the experimental curve has been extrapolated based on a curve fit of the pre-flutter data. Above the flutter speed, the motion is a rapidly divergent oscillation.

The imaginary part of the eigenvalue relates directly to the frequencies of oscillation for the system. Figure 7 shows how the pitch and plunge frequencies of the numerical

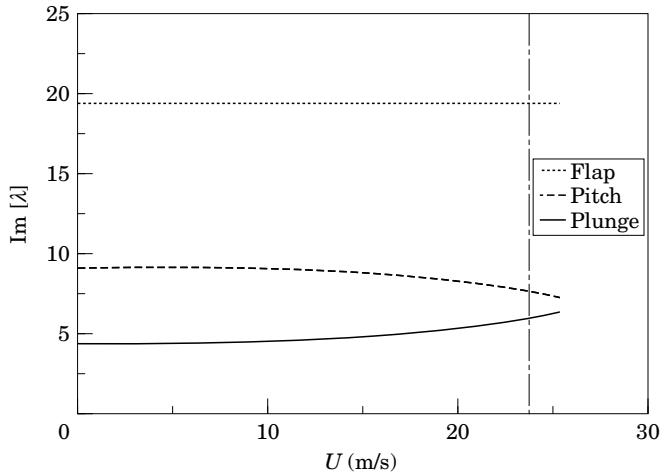

Figure 7. Numerical frequencies of oscillation for the linear system. The numerical flutter boundary is indicated by the vertical line.

model begin to approach each other as the system nears the flutter boundary. The experimental system shows a similar response, which is characterized by a flutter frequency that is between the pitch and plunge natural frequencies. It is also clear from the damping figures that the experimental and numerical systems exhibit the same qualitative behavior.

11.2. Flutter Test of the Nonlinear System

Comparisons between theory and experiment have been made for varying amounts of control surface freeplay. Three freeplay configurations are studied experimentally, corresponding to freeplay regions of ±1·15°, ±1·83° and ±2·12° (Gap 1, Gap 2 and Gap 3, respectively). The initial pitch angle of the model is zero. The model is placed in the wind tunnel such that the control surface is resting at one edge of the freeplay region. As the airflow in the tunnel is increased, this nonzero initial condition in the flap serves to excite the system, causing the wing to settle into a steady-state limit cycle. Transients are allowed to decay, and the motion of each degree of freedom is recorded in the form of time histories. The freestream velocity is slowly increased to a new value, and the process is repeated. The behavior of the system is examined at a variety of freestream conditions below the linear flutter speed. A similar path-following approach is used numerically, and all of the experimental and numerical results shown in Figure 8 are obtained by path-following.

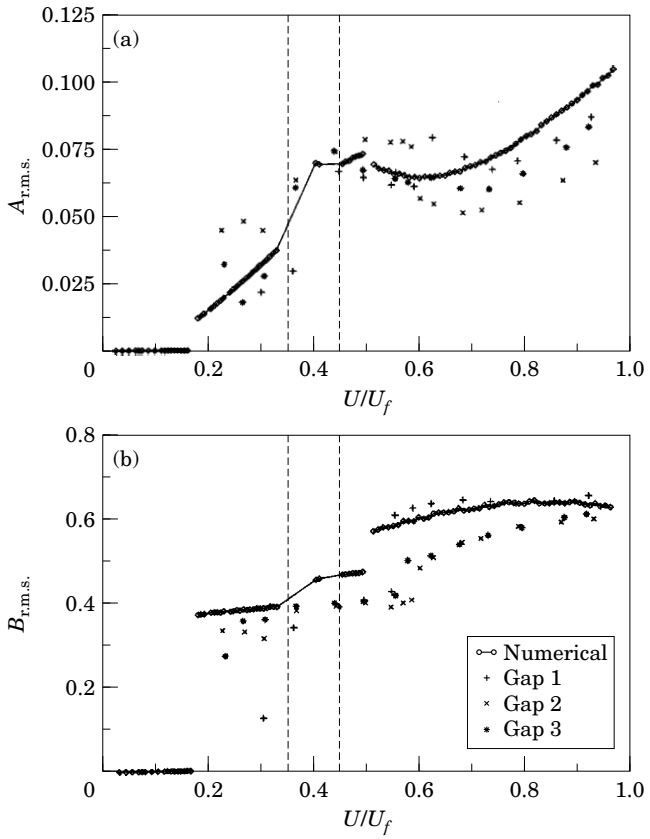

Figure 8. Numerical (lines) and experimental (points) normalized steady-state r.m.s. amplitude for the (a) pitch and (b) flap displacements. Symbols are the same for (a) and (b).

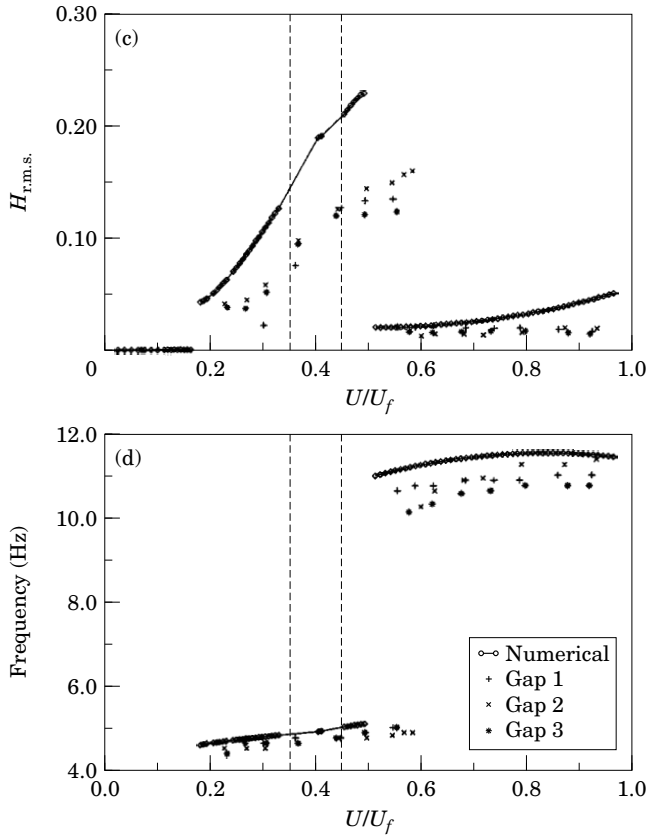

Figure 8 (*cont*). (c) Normalized stready-state r.m.s. plunge amplitude and (d) steady-state frequency; symbols as in (a) and (b).

It can be shown analytically that the response of the nonlinear systems scale with the size of the freeplay region. As a result, the numerical results, lie on a "universal" curve. The amplitude data for the nonlinear systems have been normalized by the size of the freeplay region and by the airfoil semi-chord, in the case of the plunge data. The amplitudes shown are based on root-mean square (r.m.s.) calculations over several complete cycles of the numerical and experimental steady-state time histories. Equation (7) was used to obtain the r.m.s. amplitudes:

$$\text{Amp}_{\text{r.m.s.}} = \sqrt{\frac{1}{\text{T}} \sum_{i=1}^{i=n} y_i^2 (\Delta t)_i}. \tag{7}$$

Since the motion within the freestream regime from approximately $0{\cdot}32U_f$ to $0{\cdot}44U_f$ is predominantly nonperiodic, the same definition for the r.m.s. amplitude cannot be used. Therefore, where points are plotted on the numerical curves in Figure 8(a)–(d), the motion can be assumed purely periodic, and the sections in which discrete points do not appear can be assumed nonperiodic.

Four distinct regions of pre-flutter steady-state oscillatory behavior are found experimentally, three of which are seen most clearly in Figure 8(b). For velocities between 0 and approximately 18% of the numerical linear flutter speed (23% of the experimental), giving the model an initial disturbance results in oscillations which damp out to zero fairly quickly. At $U \approx 0{\cdot}18U_f(0{\cdot}23U_f)$, there is a discrete jump from the

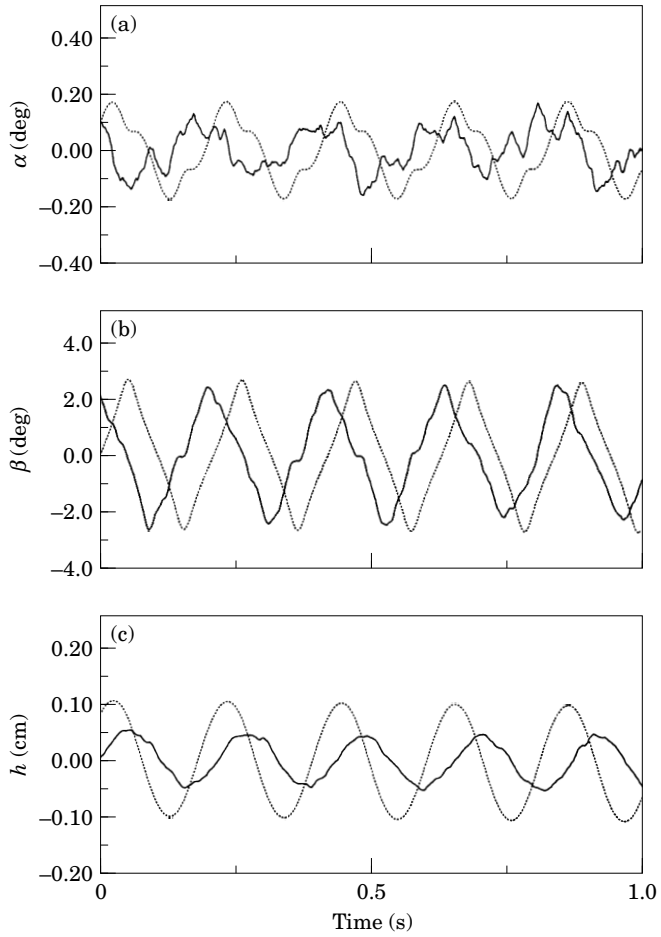

Figure 9. Experimental (solid) and numerical (dotted) (a) pitch, (b) flap and (c) plunge time histories for the low frequency limit-cycle behavior in the period-1 flap region for Gap 3, $\delta = \pm 2{\cdot}12°$; $U = 0{\cdot}27U_f$.

rest state to a low frequency limit cycle that is characterized by simple periodic oscillations in the control surface degree of freedom. Figure 9 shows an example of the experimental and numerical time series for this limit-cycle behavior. There is a slight difference between the oscillation frequencies of the two models [see Figure 8(d)], but the numerical results do predict both the qualitative and quantitative behavior found experimentally fairly accurately. Note that all of the time series presented in this section are for an arbitrary 1 s window which is applied well after both the numerical and experimental systems have reached steady-state. The time series shown in Figure 9 is phase-shifted so that the nature of the two responses can be seen. Since there are differences in the frequencies of oscillation between the numerical and experimental models, it is not necessary to pay especially close attention to the relative phases of the corresponding time series.

The system displays the simple low frequency behavior until the speed reaches approximately 35% (37%) of the linear flutter speed. At this point, the system loses periodicity over a window of freestream conditions, indicated by the vertical lines in Figure 6. At approximately 44% (48%) the motion again becomes periodic and the flap motion settles into a more complex low frequency limit cycle. The transition to the

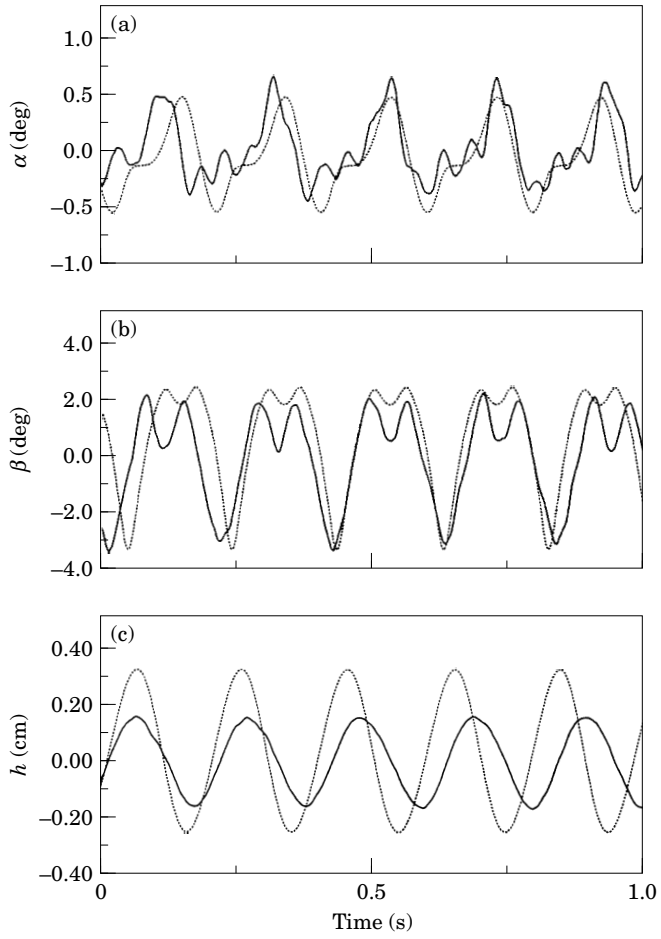

Figure 10. Experimental (solid) and numerical (dotted) (a) pitch, (b) flap and (c) plunge time histories for the low frequency limit cycle behavior in the period-2 flap region for Gap 3, $\delta = \pm 2{\cdot}12°$; $U = 0{\cdot}49U_f$.

more complex flap motion results in an increased amplitude in all three degrees of freedom, as seen in Figure 8(a)–(c).

Characteristic experimental and numerical time series for the flap motion at the end of the transition region are given in Figure 10. A wide variety of initial disturbances were applied to the experimental system and, in each case, the system settled into the same limit-cycle behavior. Due to the potential danger of damaging the experimental model, no excessively large initial conditions were examined. The limit cycle shown in Figure 10 is also found to be the only stable limit cycle over the same range of freestream velocities in the theoretical model.

At a velocity of approximately $0{\cdot}50U_f(0{\cdot}55U_f)$, there is another abrupt change in the systems behavior. The low frequency limit cycle suddenly becomes unstable, and the system is attracted to a stable, high-frequency limit cycle. There is a dramatic drop in the plunge amplitude at this point. The pitch amplitude also drops at this point and then grows again as the speed increases, while the flap amplitude jumps up and remains fairly constant (see Figure 8). Figure 11 shows that the high frequency flap motion

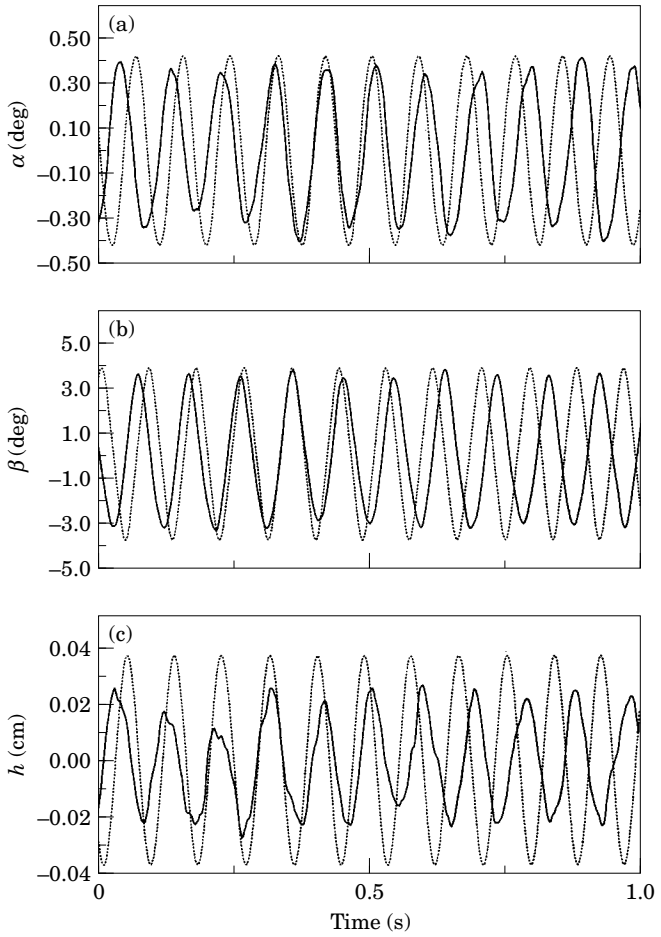

Figure 11. Experimental (solid) and numerical (dotted) (a) pitch, (b) flap and (c) plunge time histories for the high frequency limit cycle behavior in the period-1 flap region for Gap 3, $\delta = \pm 2{\cdot}12°$; $U = 0{\cdot}73U_f$.

returns to a "simple" periodic oscillation. Again, a number of perturbations were applied, each resulting in the same-limit-cycle behavior. However, shortly after the onset of this high frequency limit cycle oscillation, the transient oscillations are characteristic of the more complex flap motion that is present at the high velocity end of the low frequency regime ($0{\cdot}35U_f < U < 0{\cdot}55U_f$). From these results, it is concluded, experimentally, that the limit cycle shown in Figure 10 has become unstable. The high frequency limit cycle is observed for velocities between 55% and 93% of the experimental linear flutter speed. At higher speeds, the motion becomes divergent. (Note: Tests were not performed at speeds higher than $U \approx 0{\cdot}93U_f$ due to the danger of destroying the experimental model.) Numerical simulations for this set of system parameters indicates that the nonlinear divergent flutter speed is within 2% of the linear boundary. Previous studies have shown, though, that the divergent flutter boundary for systems with freeplay nonlinearities is a function of the initial disturbance. That is, the divergent flutter speed may decrease as the initial disturbance to the system increases (Breitbach 1977; Woolston *et al.* 1957; McIntosh *et al.* 1981).

12. CONCLUSIONS

The state-space model developed by Edwards *et al.* (1979) representing the linear three-degree-of-freedom typical section has been successfully adapted to include structural freeplay. Using a standard state-space approximation to Theodorsen aerodynamics for two-dimensional incompressible flow and applying Hénon's method to the numerical integration of a piecewise linear system, a robust numerical model for predicting linear and nonlinear flutter behavior has been constructed and verified experimentally. As shown in the experimental part of this paper, the eight-dimensional model accurately predicts, both qualitatively and quantitatively, the nonlinear behavior of the experimental model tested in the wind tunnel. The state-space representation of the system will allow for development of a variety of linear control algorithms which can be applied to both the numerical and experimental models in order to gain insight into the dangers of neglecting structural freeplay when designing a flutter suppression control system.

An experimental model of the three degree-of-freedom aeroelastic typical section has been built that successfully simulates a two-dimensional flowfield. The model allows for easy implementation of varying degrees of control surface freeplay. The results presented in this paper show that the model is capable of displaying all types of nonlinear behavior predicted theoretically. The experiments conducted on the limit-cycle behavior of the typical section have also shown that the system parameters can be affected as a result of the fatigue associated with extended oscillatory motion. While the problem may be magnified in the context of the wind tunnel testing, fatigue is still a very real concern in actual flight situations, where structural nonlinearities are unavoidable. Earlier versions of this experimental model also showed that a slight change in some of the system parameters could lead to other nonlinear phenomena, such as coexisting stable limit cycles. This behavior was also predicted theoretically.

It should be noted that both the experimental and numerical work presented in this paper serve as a verification and foundation for the next stage of this project, which is focused on the effects of structural nonlinearities on a linear control system. A control system will be added to the experimental model to allow for prescribed movement of the control surface. Specific control algorithms will be formulated based on the nominal linear system, using the state-space model discussed in this paper. Examples of previous work in aeroelastic control are given in Karpel (1982), Noll *et al.* (1984), Khargonekar & Rotea (1991), Özbay & Bachmann (1994) and Lin *et al.* (1995).

ACKNOWLEDGEMENTS

This work was supported under the AFOSR Grant "Nonlinear Dynamics and Control in Aeroelasticity", including an AASERT award for the support of MDC, and a NASA Langley Grant "Flutter of Wing and Control Surface with Freeplay". Dr C. I. "Jim" Chang and Mr Stan Cole are respective grant monitors.

References

Bayly, P. V. & Virgin, L. N. 1991 Chaotic rattling of a piecewise nonlinear oscillator. ASME 91-WA-DSC-17.

Breitbach, E. 1977 Effects of structural non-linearities on aircraft vibration and flutter. AGARD Tech. Rep. 665.

CONNER, M. D., DONESCU, P. & VIRGIN, L. N. 1996a On the global convergence characteristics of numerically evaluated jacobian matrices. *Nonlinear Dynamics* **10,** 165–174.
CONNER, M. D., VIRGIN, L. N. & DOWELL, E. H. 1996b Accurate numerical integration of state-space models for aeroelastic systems with freeplay. *AIAA Journal* **34,** 2202–2205.
DENNIS, JR., J. E. & SCHNABEL, R. B. 1983 *Numerical Methods for Unconstrained Optimization and Nonlinear Equations. Englewood Cliffs,* New Jersey: Prentice-Hall.
EDWARDS, J. W., ASHLEY, H. & BREAKWELL, J. V. 1979 Unsteady aerodynamic modeling for arbitrary motions. *AIAA Journal* **17,** 365–374.
HAUENSTEIN, A. J., ZARA, J. A. EVERSMAN, W. & QUMEI, I. 1992 Chaotic and nonlinear dynamic response of aerosurfaces with structural nonlinearities. AIAA-92-2547-CP.
HÉNON, M. 1982 On the numerical computation of Poincaré maps. *Physica* **5D,** 412–414.
KOUSEN, K. A. & BENDIKSEN, O. O. 1994 Limit cycle phenomena in computational transonic aeroelasticity. *Journal of Aircraft* **31,** 1257–1263.
LAURENSON, R. M. & TRN, R. M. 1980 flutter analysis of missile control surfaces containing structural nonlinearities. *AIAA Journal* **18,** 1245–1251.
LEE, B. H. K. & DESROCHERS, J. 1987 Flutter analysis of a two-dimensional air-foil containing structural nonlinearities. National Aeronautical Establishment—Aeronautical Report LR-618, National Research Council (Canada) No. 27833.
LEE, B. H. K. & LEBLANC, P. 1986 Flutter analysis of a two-dimensional airfoil with cubic nonlinear restoring force. National Aeronautical Establishment—Aeronautical Note—36, National Research Council (Canada) No. 2543.
LIN, W.-B. & CHENG, W.-H. 1993a Nonlinear flutter of loaded lifting surfaces (I). *Journal of the Chinese Society of Mechanical Engineers* **14,** 446–455.
LIN, W.-B. & CHENG, W.-H. 1993b. Nonlinear flutter of loaded lifting surfaces (II). *Journal of the Chinese Society of Mechanical Engineers* **14,** 456–466.
MCINTOSH, JR, S. C., REED, JR., R. E. & RODDEN, W. P. 1981 Experimental and theoretical study of nonlinear flutter. *Journal of Aircraft* **18,** 1057–1063.
MURPHY, K. D., BAYLY, P. V., VIRGIN, L. N. & GOTTWALD, J. A. 1994 Measuring the stability of periodic attractors using perturbation-induced transients: applications to two non-linear oscillators. *Journal of Sound and Vibration* **172,** 85–102.
PRICE, S. J., ALIGHANBARI, H. & LEE, B. H. K. 1995 The aeroelasatic response of a two-dimensional airfoil with bilinear and cubic structural nonlinearities. *Journal of Fluids and Structures* **9,** 175–193.
PRICE, S. J., LEE, B. H. K. & ALIGHANBARI, H. 1994 Postinstability behavior of a two-dimensional airfoil with a structural nonlinearity. *Journal of Aircraft* **31,** 1395–1401.
SHEN, S. F. 1959 An approximate analysis of nonlinear flutter problems. *Journal of the Aero/Space Sciences* **26,** 25–45.
TANG, D. M. & DOWELL, E. H. 1992 Flutter and stall response of a helicopter blade with structural nonlinearity. *Journal of Aircraft* **29,** 953–960.
THEODORSEN, T. & GARRICK, I. E. 1941 Flutter calculations in three degrees of freedom. NACA Report No. 741.
THOMSON, W. T. 1988 *Theory of Vibration with Applications,* 3rd ed. Englewood Cliffs, New Jersey: Prentice-Hall.
WOOLSTON, D. S., RUNYAN, H. L. & ANDREWS, R. E. 1957 An investigation of effects of certain types of structural nonlinearities on wing and control surface flutter. *Journal of the Aeronautical Sciences,* **24,** 57–63.
WOOLSTON, D. S., RUNYAN, H. L. & BYRDSONG, T. A. 1955 Some effects of system nonlinearities in the problem of aircraft flutter. NACA T.N. 3539.
YANG, Z. C. & ZHAO, L. C. 1988 Analysis of limit cycle flutter of an airfoil in incompressible flow. *Journal of Sound and Vibration* **123,** 1–13.

APPENDIX A: PARAMETER DEFINITIONS, AND VALUES FOR THE EXPERIMENTAL SYSTEM

The following system parameter definitions have been adapted from Theodorsen (1935), in which ρ is the mass of air per unit of volume, b the half-chord of wing, and M the mass of wing per unit of length.

S_α, S_β: static moments of wing per unit length of wing-aileron (relative to a) and aileron (relative to c), respectively.

I_α, I_β: moments of inertia per unit length of wing-aileron and aileron about a and c, respectively.

C_α, C_β: torsional stiffness per unit length of wing and aileron around a and c, respectively.

C_h: stiffness of wing in deflection per unit length.

$K_{\alpha,\beta} = \dfrac{C_{\alpha,\beta}}{Mb^2}$ *reduced* torsional stiffnesses.

$K_h = \dfrac{C_h}{M}$ *reduced* stiffness in deflection.

$\kappa = \dfrac{\pi\rho b^2}{M}$ the ratio of the mass of a cylinder of air having a diameter equal to the chord of the wing to the mass of the wing, both per unit span.

$r_\alpha = \sqrt{\dfrac{I_\alpha}{Mb^2}}$ the radius of gyration divided by b.

$x_\alpha = \dfrac{S_\alpha}{Mb}$ the center of gravity distance of the wing from a, divided by b.

TABLE A.1
System parameters for the experimental system

Geometric parameters	
Chord	0·254 m
Span	0·52 m
Semi-chord, b	0·127 m
Elastic axis, a w/r/t b	−0·5
Hinge line, c w/r/t b	0·5
Mass parameters	
Mass of wing	0·62868 kg
Mass of aileron	0·18597 kg
Mass/length of wing-aileron	1·558 kg/m
Mass of support blocks	0·47485 × 2 kg
Inertial parameters	
S_α (per span)	0·08587 kg m
S_β (per span)	0·00395 kg m
x_α	0·434
x_β	0·01996
I_α (per span)	0·01347 kg m^2
I_β (per span)	0·0003264 kg m^2
r_α	0·7321
r_β	0·11397
κ	0·03984
Stiffness parameters	
K_α (per span)	1486 l/s^2
K_β (per span)	155 1/s^2
K_h (per span)	1809 l/s^2
Damping parameters	
ζ_α (log-dec)	0.01626
ζ_β (log-dec)	0·0115
ζ_h (log-dec)	0·0113

$\bar{\omega}_\alpha = \sqrt{\frac{C_\alpha}{I_\alpha}}$ the uncoupled natural frequency of torsional vibration around *a.*

$r_\beta = \sqrt{\frac{I_\beta}{Mb^2}}$ the *reduced* radius of gyration of the aileron divided by *b,* that is, the radius at which the entire mass of the airfoil would have to be concentrated to give the moment of inertia of the aileron, I_β.

$x_\beta = \frac{S_\beta}{Mb}$ the *reduced* center of gravity distance from *c.*

$\bar{\omega}_\beta = \sqrt{\frac{C_\beta}{I_\beta}}$ the uncoupled natural frequency of torsional vibration of the aileron around *c.*

$\bar{\omega}_h = \sqrt{\frac{C_h}{m}}$ the uncoupled natural frequency of the wing in deflection.

APPENDIX B: NOMENCLATURE

The following is a list of symbols used in the body of the paper.

Scalars

A	nondimensional nonlinear pitch displacement (α/δ)
b	semi-chord
B	nondimensional nonlinear flap displacement (β/δ)
h	plunge displacement
H	nondimensional nonlinear plunge displacement $(h/(b\delta))$
m	modal mass
T	period of oscillation
U	freestream velocity
y	dummy displacement variable
α	pitch displacement
β	control surface displacement
δ	size of freeplay region
Δt	time step
ω	natural frequency
ζ	modal damping ratio

Vectors & Matrices

$\mathbf{a}$	"offset" vector associated with freeplay
$\mathbf{A}$	state coefficient matrix
$\mathbf{B}$	control coefficient matrix
$\mathbf{D}, \mathbf{E}_1, \mathbf{E}_2, \mathbf{F}_a$	aerodynamic approximation matrices
$\mathbf{G}$	control input submatrix
$\mathbf{K}$	stiffness submatrix
$\mathbf{M}$	mass submatrix
$\mathbf{x}$	state vector $[\alpha, \beta, h]^{\mathrm{T}}$
$\hat{\mathbf{x}}$	full state vector $[x, \dot{x}, x_a]^{\mathrm{T}}$

Subscripts

f	linear flutter value
mod	modal value
r.m.s.	root-mean-square value
s	structural component of state-space matrices
tot	total value, including structural and aerodynamic components
h, α, β	plunge, pitch, control surface